

## Upper-branch thermal Hall effect in quantum paramagnets

Bowen Ma,<sup>1,2,3</sup> Z. D. Wang,<sup>2</sup> and Gang V. Chen<sup>1,3,\*</sup><sup>1</sup>*International Center for Quantum Materials, School of Physics, Peking University, Beijing 100871, China*<sup>2</sup>*Department of Physics and HK Institute of Quantum Science & Technology,  
The University of Hong Kong, Pokfulam Road, Hong Kong, China*<sup>3</sup>*The University of Hong Kong Shenzhen Institute of Research and Innovation, Shenzhen 518057, China*

(Received 29 September 2023; revised 15 March 2024; accepted 21 March 2024; published 11 April 2024)

Inspired by the persistent thermal Hall effects at finite temperatures in various quantum paramagnets, we explore the origin of the thermal Hall effects from the perspective of the upper branch parts by invoking dispersive and twisted crystal field excitations. It is shown that the upper branches of the local energy levels could hybridize and form dispersive bands. The observation is that, upon time-reversal symmetry breaking by the magnetic fields, these upper branch bands could acquire a Berry curvature distribution and contribute to the thermal Hall effect even in the paramagnetic regime. As a proof of principle, we consider the setting on kagomé lattice with one ground-state singlet and an excited doublet, and show this is indeed possible. We expect this effect to be universal and that it has no strong connection with the underlying lattice. Although the thermal Hall signal can be contributed from other sources such as phonons and their scattering in the actual materials, we discuss the application to the relevant quantum materials.

DOI: [10.1103/PhysRevResearch.6.023044](https://doi.org/10.1103/PhysRevResearch.6.023044)

## I. INTRODUCTION

Recently, thermal Hall transports have been widely used to explore the properties of elementary excitations in correlated quantum materials. In Mott insulating systems where the relevant excitations are charge neutral, the thermal Hall effect plays an important role in deciphering the Berry curvature properties of the excitations [1]. For quantum spin liquids, half-quantized thermal Hall conductivity is one smoking-gun result for the gapped Kitaev spin liquid with the chiral Majorana edge mode [2], and might have been observed in  $\alpha$ -RuCl<sub>3</sub> [3,4]. The thermal Hall effects could reflect the intrinsic matter-gauge coupling and the Berry curvature properties of the emergent exotic quasiparticles in different spin liquids [1]. As a probe of the magnetic excitations, the thermal Hall effect is found to be useful in more conventional magnets. The magnon thermal Hall effects [5–9] were widely studied in many ordered magnets. In a class of magnets known as “dimerized magnets” where the ground state is approximately given as the product of the spin-singlet dimers on the bonds with stronger exchanges, the spin-triplet excitations, known as “triplons,” can propagate via interdimer couplings and form triplon bands. These triplon bands can acquire non-trivial Berry curvatures and even finite Chern numbers once the anisotropic interaction such as the Dzyaloshinskii-Moriya

interaction is introduced [10,11]. This leads to interesting behaviors in the triplon thermal Hall effect.

Thermal Hall conductivity has been measured in several representative quantum magnets such as Tb<sub>2</sub>Ti<sub>2</sub>O<sub>7</sub> [12], Pr<sub>2</sub>Zr<sub>2</sub>O<sub>7</sub> [13], Pr<sub>2</sub>Ir<sub>2</sub>O<sub>7</sub> [14], and Na<sub>2</sub>Co<sub>2</sub>TeO<sub>6</sub> [15,16]. One common feature of these quantum magnets is that, due to the combination of the crystal electric field (CEF) and the spin-orbit coupling (SOC), the magnetic ions have a relatively large local physical Hilbert space with a series of local energy levels [17]. We take the well-known compound Tb<sub>2</sub>Ti<sub>2</sub>O<sub>7</sub> as an example [12,18,19]. Via the SOC, the Tb<sup>3+</sup> ion has a  $J = 6$  local moment. The 13-fold degeneracy is further split by the CEF into multiple singlets and doublets. As the thermal Hall transport in Tb<sub>2</sub>Ti<sub>2</sub>O<sub>7</sub> was measured up to 142 K and 10 T [12], at this temperature scale, the second excited doublet (at 1.41 meV) has already been thermally activated. The CEF multiplets could then make a significant impact on the physics of those quantum magnets [20]. In addition, the CEF levels at 10–20 meV would be thermally populated. The 10 T magnetic field reorganizes these CEF states and splits the doublets. For the activated CEF states, the 10 T field could create a Zeeman splitting of about 20–40 K. The previous work that studies the monopole thermal Hall effect [21] from the ground-state doublets in the quantum ice regime [19] certainly cannot be extended to such high temperatures and large magnetic field regimes. Thus, these two ingredients, i.e., the thermal activation and the field splitting or hybridization of the CEF states, indicate that one should seriously consider the involvement of these excited CEF states in thermal transports. Similar physics should generally occur in other rare-earth magnets as well as other multiflavor Mott insulators [1,22]. This aspect for the multiflavor Mott insulators is quite different from the cuprate system where the local Hilbert space in a large range of energy

\*chenxray@pku.edu.cn

Published by the American Physical Society under the terms of the [Creative Commons Attribution 4.0 International license](https://creativecommons.org/licenses/by/4.0/). Further distribution of this work must maintain attribution to the author(s) and the published article's title, journal citation, and DOI.

scale is a spin-1/2 local moment from the  $e_g$  electrons and the large thermal Hall signal was observed in cuprate [23,24].

If one views the CEF excitations in the multiflavor Mott insulators as generalized triplons with respect to the CEF ground state, this view bridges this series of quantum magnets with the dimerized magnets. One immediate outcome is that these generalized triplons, similar to the topological excitations in the excitonic magnets [25], should in principle possess the Berry curvatures in the magnetic field and contribute to the thermal Hall conductivity at the relevant temperature regime. In Ref. [26], the upper branch magnetism from the excited CEF states was understood when the CEF gap is comparable to the exchange interaction between the CEF states of the neighboring sites. Therefore, the thermal Hall effect from the generalized triplons is dubbed “upper branch thermal Hall effect.”

The remaining parts of the paper are organized as follows. In Sec. II, we formulate the effective spin model for the kagomé lattice. In Sec. IV, we perform the flavor wave theory analysis in the quantum paramagnetic phase and establish the excitations in this phase. In Sec. V, we explain the topological properties of the bands and establish the thermal Hall transports of the generalized triplons. Finally, we discuss the experiments in the relevant materials.

## II. EFFECTIVE SPIN MODEL FROM CRYSTAL FIELD STATES

We begin from the single-ion limit of the spin-orbit-coupled Mott insulators, where the  $2J + 1$  states of the local  $J$  moment of the magnetic ions naturally split into the ground state and the excited multiplets under the CEF effects. Since we are mostly concerned about the excited CEF states, to simplify the problem, we assume the CEF ground state is a singlet and the first excited CEF states form a doublet, and neglect the effects from other higher excited CEF states. The three states of the local moment are then described by an effective spin  $S = 1$  with an on-site anisotropic term  $\sum_i \eta (\hat{\mathbf{z}}_i \cdot \mathbf{S}_i)^2$  and  $\eta > 0$ , where  $\hat{\mathbf{z}}_i$  is defined along the local coordinate of the CEF environment for each sublattice. The spin-1 moment differs from the pseudospin-1/2 moment that is often used to describe Kramers or non-Kramers doublets in many rare-earth magnets. In our design, the lower singlet corresponds to  $S_i^z = 0$ , and the upper doublet correspond to  $S_i^z = \pm 1$ . In most cases in which we are interested, the lower singlet and the upper doublet can be connected by the ladder operator of the original  $\hat{\mathbf{J}}$  operators, i.e., the local ladder operators have nonvanishing matrix elements between the singlet and the doublet. Thus, all three local components of  $\mathbf{S}_i$  are odd under time reversal.

Although the upper branch thermal Hall effect arises from the CEF states whose interactions depend on the CEF wave functions and lattice symmetries, the underlying lattice is needed but usually not required to be unique, which is a bit similar to the magnon or phonon thermal Hall effects. Thus, for concreteness, we consider the setting on a kagomé lattice as shown in Fig. 1, which shares many common features with those actively investigated pyrochlore quantum magnets. Experimentally, this kagomé setup can be established by applying the [111] magnetic field on the pyrochlore magnets, or

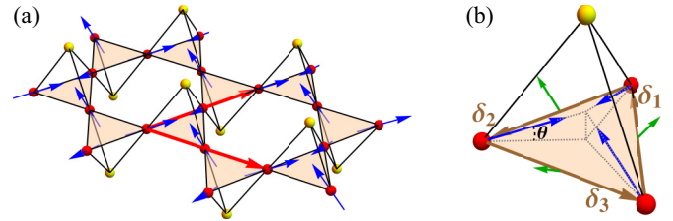


FIG. 1. (a) The tripod kagomé lattice with the effective spins on the red sites. The blue arrows denote the local Ising  $z$  axes. The red vectors are the basis vectors  $\mathbf{a}_1 = a(1, 0)$  and  $\mathbf{a}_2 = a(1/2, \sqrt{3}/2)$ . (b) The tripod unit cell. The Ising  $z$  axes have a canting angle  $\theta$  with the kagomé plane. The green arrow normal to each bond shows the DM vectors with in-plane component  $D_\rho$  and out-of-plane component  $D_z$ . The neighboring bonds are  $\delta_1 = a(-1/4, \sqrt{3}/4)$ ,  $\delta_2 = a(-1/4, -\sqrt{3}/4)$ , and  $\delta_3 = a(1/2, 0)$ .

naturally occurs in the tripod kagomé magnets [27,28]. With the symmetry of the kagomé lattice, for the three sublattices denoted as  $m = 1, 2, 3$ , we have the easy axes with an out-of-plane canting angle  $\theta$  as

$$\hat{\mathbf{z}}_m = \left( \sin \frac{2\pi m}{3} \cos \theta, -\cos \frac{2\pi m}{3} \cos \theta, \sin \theta \right), \quad (1)$$

which will be adopted in the anisotropic term for the local effective spin-1 variables.

Under this effective spin-1 representation, the interaction between the neighboring multiplets is expressed as spin exchange coupling. We thus consider an exchange model that is quadratic in the effective spin-1 components as

$$H_{\text{ex}} = \sum_{\langle ij \rangle} \sum_{\alpha\beta} \mathbf{S}_i^\alpha \Lambda_{ij}^{\alpha\beta} \mathbf{S}_j^\beta, \quad (2)$$

where  $\mathbf{S}_i^\alpha$  denotes the  $\alpha$  component of  $\mathbf{S}_i$  in the global coordinate, and the exchange coupling matrix is given as

$$\Lambda_{ij} = \begin{pmatrix} J & D_{ij}^z & -D_{ij}^y \\ -D_{ij}^z & J & D_{ij}^x \\ D_{ij}^y & -D_{ij}^x & J \end{pmatrix}, \quad (3)$$

including both symmetric Heisenberg exchange coupling  $J$  and the antisymmetric Dzyaloshinskii-Moriya (DM) interaction [29,30]  $\mathbf{D}_{ij} = (D_{ij}^x, D_{ij}^y, D_{ij}^z)$ .

The full effective spin Hamiltonian under an out-of-plane magnetic field can be written as

$$H = \sum_{\langle ij \rangle} [J \mathbf{S}_i \cdot \mathbf{S}_j + \mathbf{D}_{ij} \cdot (\mathbf{S}_i \times \mathbf{S}_j)] + \sum_i \eta (S_i^z)^2 - \sum_i B (\hat{\mathbf{z}} \cdot \hat{\mathbf{z}}_i) S_i^z, \quad (4)$$

with  $B$  the Zeeman splitting. Although the Zeeman coupling could involve all the spin components, only the Zeeman coupling to the local  $z$  component  $S_i^z \hat{\mathbf{z}}_i$  is considered for simplicity. Moreover, more complicated spin interactions, such as pseudodipolar interactions, and higher-order spin interactions could be present. This kind of interaction between the upper doublets of three neighboring sites has the form of a four-spin interaction [26]. According to Moriya’s rule [29], the DM

vectors are further constrained to be

$$\begin{aligned} \mathbf{D}_{12} &= -\mathbf{D}_{21} = (0, -D_p, D_z), \\ \mathbf{D}_{23} &= -\mathbf{D}_{32} = \left(\frac{\sqrt{3}}{2}D_p, \frac{1}{2}D_p, D_z\right), \\ \mathbf{D}_{31} &= -\mathbf{D}_{13} = \left(-\frac{\sqrt{3}}{2}D_p, \frac{1}{2}D_p, D_z\right), \end{aligned} \quad (5)$$

with  $D_z$  the out-of-plane component along global  $\hat{\mathbf{z}}$  direction and  $D_p = |\mathbf{D}_{ij} - D_z\hat{\mathbf{z}}|$  the in-plane component.

### III. FLAVOR-WAVE THEORY FOR QUANTUM PARAMAGNET

In the strong anisotropic limit with  $\eta > 0$ , the ground state is a simple quantum paramagnet with  $S_i^z = 0$ . With the exchange interactions  $\Lambda_{ij}^{\alpha\beta}$ , the many-body ground state depletes a bit from  $S_i^z = 0$ , which is analogous to the depletion of superfluid weight in the Bose-Einstein condensation of interacting bosons except the absence of the continuous symmetry here. The excited doublets form dispersive bands. As the ground state is a robust paramagnetic singlet, the picture does not alter much in the presence of the external magnetic fields. Since the ground state is paramagnetic without ordering, the usual Holstein-Primakoff boson representation is not suitable to describe the excitations. Instead, we regard  $S_i^z = 0, \pm 1$  as three different flavors [31,32] in the spirit of the SU(3) flavors, and invoke a linear flavor-wave representation of  $\mathbf{S}_i$  as [33]

$$\begin{aligned} S_i^z &\equiv \hat{\mathbf{z}}_i \cdot \mathbf{S}_i = b_i^\dagger b_i - \bar{b}_i^\dagger \bar{b}_i, \\ S_i^- &\equiv (\hat{\mathbf{x}}_i - i\hat{\mathbf{y}}_i) \cdot \mathbf{S}_i \approx \sqrt{2}(\bar{b}_i^\dagger + b_i), \\ S_i^+ &\equiv (\hat{\mathbf{x}}_i + i\hat{\mathbf{y}}_i) \cdot \mathbf{S}_i \approx \sqrt{2}(\bar{b}_i + b_i^\dagger), \end{aligned} \quad (6)$$

where  $(\hat{\mathbf{x}}_i, \hat{\mathbf{y}}_i, \hat{\mathbf{z}}_i)$  spans a local coordinate for site  $i$ . More details can be found in Appendix A. For the quantum paramagnet here, the boson operators  $b_i^\dagger$  and  $\bar{b}_i^\dagger$  ( $b_i$  and  $\bar{b}_i$ ) create (annihilate) a state with magnetic flavor  $S_i^z = +1$  and  $-1$ , respectively. As long as the ground state of the quantum paramagnet is stable against fluctuation so that  $\langle b_i^\dagger b_i \rangle, \langle \bar{b}_i^\dagger \bar{b}_i \rangle \ll 1$ , the higher-order effects can be ignored and the linear flavor-wave theory can remain applicable.

Due to the noncollinearity of the Ising axes of the three sublattices, one needs to rotate the spin operators in Eq. (4) into the local coordinate for different sites [34,35], and this generates the pairing of the flavor bosons. More specifically, for local Ising axis  $\hat{\mathbf{z}}_i = (\cos \theta_i \cos \phi_i, \cos \theta_i \sin \phi_i, \sin \theta_i)$ , one needs to rotate  $\mathbf{S}_i$  into the local coordinate by

$$R_i = \begin{pmatrix} \sin \theta_i \cos \phi_i & -\sin \phi_i & \cos \theta_i \cos \phi_i \\ \sin \theta_i \sin \phi_i & \cos \phi_i & \cos \theta_i \sin \phi_i \\ -\cos \theta_i & 0 & \sin \theta_i \end{pmatrix}, \quad (7)$$

as  $\mathbf{S}_i = R_i(\hat{\mathbf{x}}_i \cdot \mathbf{S}_i, \hat{\mathbf{y}}_i \cdot \mathbf{S}_i, \hat{\mathbf{z}}_i \cdot \mathbf{S}_i)^T$ . Correspondingly, the coupling matrix  $\Lambda_{ij}$  transforms as  $\tilde{\Lambda}_{ij} = R_i^T \Lambda_{ij} R_j$  so that

$$\mathbf{S}_i \Lambda_{ij} \mathbf{S}_j = (\hat{\mathbf{x}}_i \cdot \mathbf{S}_i, \hat{\mathbf{y}}_i \cdot \mathbf{S}_i, \hat{\mathbf{z}}_i \cdot \mathbf{S}_i) \tilde{\Lambda}_{ij} \begin{pmatrix} \hat{\mathbf{x}}_j \cdot \mathbf{S}_j \\ \hat{\mathbf{y}}_j \cdot \mathbf{S}_j \\ \hat{\mathbf{z}}_j \cdot \mathbf{S}_j \end{pmatrix}. \quad (8)$$

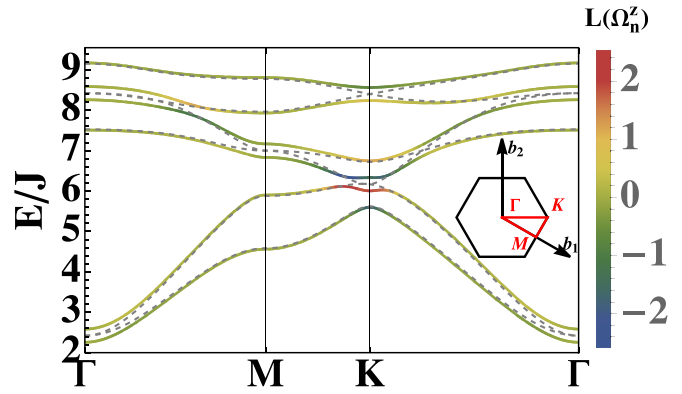


FIG. 2. The band dispersion of the doublet excitations from the linear flavor-wave theory. We set  $\sin \theta = 1/3$ ,  $\eta/J = 7.0$ ,  $\sqrt{3}D_p = \sqrt{3/2}D_z = D = 0.9J$ , and  $B/J = 0.5$  (0) for the solid (dashed) lines. The color of the solid line shows the nonzero Berry curvature in the log scale  $L(\Omega_n^z) = \text{sgn}(\Omega_n^z) \ln(1 + |\Omega_n^z|)$ . The inset shows the hexagonal Brillouin zone.

To the quadratic order of the bosonic operators, we obtain

$$\begin{aligned} H &= \sum_{\langle ij \rangle} [A_{ij}(b_i^\dagger b_j + \bar{b}_i \bar{b}_j^\dagger + b_i^\dagger \bar{b}_j^\dagger + \bar{b}_i b_j) \\ &\quad + B_{ij}(b_i b_j + \bar{b}_i^\dagger \bar{b}_j^\dagger + b_i \bar{b}_j^\dagger + \bar{b}_i^\dagger b_j) + \text{H.c.}] \\ &\quad + \sum_i [\eta(b_i^\dagger b_i + \bar{b}_i^\dagger \bar{b}_i) - B(b_i^\dagger b_i - \bar{b}_i^\dagger \bar{b}_i)], \end{aligned} \quad (9)$$

with

$$A_{ij} = \frac{1}{2}(\tilde{\Lambda}_{ij}^{xx} + \tilde{\Lambda}_{ij}^{yy} + i\tilde{\Lambda}_{ij}^{xy} - i\tilde{\Lambda}_{ij}^{yx}), \quad (10)$$

$$B_{ij} = \frac{1}{2}(\tilde{\Lambda}_{ij}^{xx} - \tilde{\Lambda}_{ij}^{yy} + i\tilde{\Lambda}_{ij}^{xy} + i\tilde{\Lambda}_{ij}^{yx}). \quad (11)$$

Therefore, after the Fourier transform, the Hamiltonian Eq. (4) needs to be written in a Bogoliubov-de Gennes (BdG) form as

$$H = \frac{1}{2} \sum_{\mathbf{k}} \Psi_{\mathbf{k}}^\dagger H_{\mathbf{k}} \Psi_{\mathbf{k}} \quad (12)$$

with

$$H_{\mathbf{k}} = \begin{pmatrix} A_{\mathbf{k}} & B_{\mathbf{k}} \\ B_{-\mathbf{k}}^* & A_{-\mathbf{k}}^* \end{pmatrix}, \quad (13)$$

and

$$\Psi_{\mathbf{k}} = (b_{1\mathbf{k}}, \bar{b}_{1\mathbf{k}}, \dots, b_{3\mathbf{k}}, \bar{b}_{3\mathbf{k}}, b_{1,-\mathbf{k}}^\dagger, \bar{b}_{1,-\mathbf{k}}^\dagger, \dots, b_{3,-\mathbf{k}}^\dagger, \bar{b}_{3,-\mathbf{k}}^\dagger)^T. \quad (14)$$

The explicit form of  $A_{\mathbf{k}}$  and  $B_{\mathbf{k}}$  can be found in Appendix B. The dispersion of the flavor-wave excitations can be determined as the positive eigenvalues of  $\Sigma_z H_{\mathbf{k}}$  [34,36], where we have

$$\Sigma_z = \sigma_z \otimes I_6, \quad (15)$$

with  $\sigma_z$  the Pauli matrix and  $I_6$  the  $6 \times 6$  identity matrix. In Fig. 2, we depict the representative dispersions in the quantum paramagnetic phase.

When  $B \neq 0$ , the bands are separated from each other due to time-reversal symmetry breaking. If the band becomes too dispersive so that the band bottom touches zero energy,

the bosons begin to condensate, and the system develops a corresponding magnetically ordered ground state other than the quantum paramagnetic state [33]. To avoid that, we work in the regime with  $\Lambda_{ij}^{\alpha\beta}$ ,  $B < \eta$  such that the quantum paramagnet remains stable throughout. The phase region of this quantum paramagnetic state and detailed discussion can be found in Appendix B.

#### IV. TOPOLOGICAL TRANSPORT OF TRIPLONS

##### A. Band topology

In magnetically ordered systems, the DM interaction or/and the noncollinear spin configuration could give rise to topological magnons with nonzero Chern numbers [7,37–39]. With the DM interactions and/or the noncollinear Ising axes in the current model, the Berry curvature of the flavor-wave excitation in the quantum paramagnet is also expected to be nonzero. In the case of the bosonic BdG Hamiltonian, the wave function of the  $n$ th band  $|\psi_{nk}\rangle$  is determined by the eigenequation

$$E_{nk}|\psi_{nk}\rangle = \Sigma_z H_{\mathbf{k}}|\psi_{nk}\rangle. \quad (16)$$

The corresponding Berry connection  $\mathcal{A}_{nk}$  and Berry curvature  $\Omega_{nk}$  is then defined as [9]

$$\mathcal{A}_{nk} = i\langle\psi_{nk}|\Sigma_z \nabla_{\mathbf{k}}|\psi_{nk}\rangle, \quad (17)$$

$$\Omega_{nk} = \nabla_{\mathbf{k}} \times \mathcal{A}_{nk}. \quad (18)$$

In two-dimensional systems, the first Chern number can then be calculated by integrating the  $z$  component of  $\Omega_{nk}$  over the Brillouin zone as

$$C_n = \frac{1}{2\pi} \sum_{\mathbf{k}} \Omega_{nk}^z. \quad (19)$$

The general analysis of the band topology with an arbitrary choice of parameters is unnecessary for our purpose. Without loss of much generality, we consider a simple case where the Ising axes  $\hat{\mathbf{z}}_i$  are all perpendicular to the kagomé plane, and the DM vectors only have out-of-plane components as  $\mathbf{D}_{12} = \mathbf{D}_{23} = \mathbf{D}_{31} = D_z \hat{\mathbf{z}}$ . With this simplification, if we perform a basis transformation as

$$u_{mk} = \frac{1}{\sqrt{2}}(b_{mk} + \bar{b}_{m,-k}^\dagger), \quad (20)$$

$$p_{mk} = i\frac{1}{\sqrt{2}}(\bar{b}_{m,-k}^\dagger - b_{mk}), \quad (21)$$

the Hamiltonian can then be written as

$$H = \frac{1}{2(2\eta)^{-1}} \sum_{\mathbf{k}} (\mathbf{p}_{\mathbf{k}}^\dagger - iB\eta^{-1}\mathbf{u}_{\mathbf{k}}^\dagger)(\mathbf{p}_{\mathbf{k}} + iB\eta^{-1}\mathbf{u}_{\mathbf{k}}) + \frac{1}{2} \sum_{\mathbf{k}} \mathbf{u}_{\mathbf{k}}^\dagger (4M_{\mathbf{k}} - 2B^2\eta^{-1})\mathbf{u}_{\mathbf{k}} \quad (22)$$

with

$$M_{\mathbf{k}} = \frac{\eta}{2}I_3 + \begin{pmatrix} 0 & 2\tilde{J} \cos \mathbf{k}_3 & 2\tilde{J}^* \cos \mathbf{k}_2 \\ 2\tilde{J}^* \cos \mathbf{k}_3 & 0 & 2\tilde{J} \cos \mathbf{k}_1 \\ 2\tilde{J} \cos \mathbf{k}_2 & 2\tilde{J}^* \cos \mathbf{k}_1 & 0 \end{pmatrix}, \quad (23)$$

where  $\tilde{J} = J + iD_z = |\tilde{J}|e^{-i\phi/3}$ ,  $\mathbf{k}_m = \mathbf{k} \cdot \delta_m$ ,  $\mathbf{u}_{\mathbf{k}} = (u_{1\mathbf{k}}, u_{2\mathbf{k}}, u_{3\mathbf{k}})$ ,  $\mathbf{p}_{\mathbf{k}} = (p_{1\mathbf{k}}, p_{2\mathbf{k}}, p_{3\mathbf{k}})$ , and

$$[u_{m\mathbf{k}}^\dagger, p_{m'\mathbf{k}'}] = i\delta_{mm'}\delta_{\mathbf{k}\mathbf{k}'}. \quad (24)$$

The Hamiltonian Eq. (22) is an analog of a phononic system on the kagomé lattice with a mass  $(2\eta)^{-1}$  and a dynamical matrix  $4M_{\mathbf{k}} - 2B^2\eta^{-1}$ . In Appendix C, we show that the wave function of this phononic Hamiltonian remains unchanged when  $B \rightarrow 0^+$  and thus band Chern numbers can be fully determined by  $M_{\mathbf{k}}$  even with finite  $B$ . Interestingly,  $M_{\mathbf{k}}$  is topologically equivalent to the chiral spin Hamiltonian [40] or topological magnonic Hamiltonian [6] on kagomé lattice, where the inequivalence between the honeycomb plaquette and the triangular plaquette leads to a nonzero  $\phi$  flux. Therefore, there is a  $SU(3) \oplus SU(3)$  band topology where the Chern numbers of the three bands with flavor  $\pm 1$  are determined by a  $SU(3)$  structure [41] as  $[\mp \text{sgn}(\sin \phi), 0, \pm \text{sgn}(\sin \phi)]$  from bottom to top.

In a more general situation with noncollinear Ising axes, we choose  $\eta = 7J$  and assume the system further respects a  $O_h$  point group symmetry that is inherited from the parent pyrochlore lattice so that  $D_z = \sqrt{2}D_p = \sqrt{2/3}D$ . After numerically computing the band Chern number in the discretized momentum space [42], we obtain a topological phase diagram for the lower three bands shown in Fig. 3. The full diagram for all six bands can be found in Appendix B. We find that, due to the mixing of the two flavors in the global coordinate, the  $SU(3) \oplus SU(3)$  topology is enriched with varying intrinsic couplings as well as the external magnetic field.

From the analytical calculation and numerical study above, we can see that nontrivial Berry physics of the excited doublets in our model originates from the noncancellation of the flux in the kagomé lattice, and thus we believe that similar nontrivial topology for even more general multiplet excitations will also occur in various lattices with inequivalent plaquettes such as honeycomb [43], checkerboard [44,45], and bulk [33] or thin-filmed [46] pyrochlore lattices.

##### B. Thermal Hall effects

Semiclassically, with the finite Berry curvature, the wave packet of the excitations will experience an anomalous velocity from  $\Omega$  as [47,48]

$$\dot{\mathbf{r}}_n = \frac{1}{\hbar} \frac{\partial E_{nk}}{\partial \mathbf{k}} - \dot{\mathbf{k}} \times \Omega_{nk}, \quad (25)$$

where  $\mathbf{r}_n$  is the packet center of the  $n$ th wave function. If a longitudinal temperature gradient  $\nabla_y T$  is applied across the material, the transverse motion of the excitations from the anomalous velocity term will lead to some Hall-like transport signals. In the case of thermal Hall effects, the excitations carrying different energies will experience different anomalous velocities, and thus lead to a transverse temperature difference. From the theoretical side, the associated thermal Hall conductivity  $\kappa_{xy}$  of bosonic excitations can be derived from linear response theory as [49,50]

$$\kappa_{xy} = -\frac{k_B^2 T}{\hbar V} \sum_{n,\mathbf{k}} \left\{ c_2[g(E_{nk})] - \frac{\pi^2}{3} \right\} \Omega_{nk}^z, \quad (26)$$

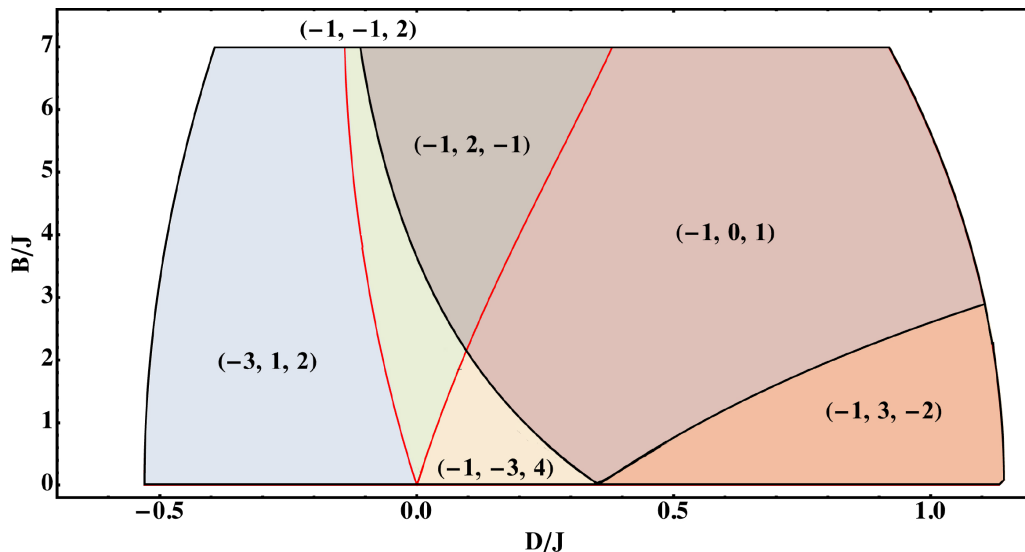


FIG. 3. Diagram of Chern number distributions for the lower three bands. The Chern numbers are listed from bottom to top. We set  $\sin \theta = 1/3$ ,  $\eta/J = 7.0$ ,  $\sqrt{3}D_p = \sqrt{3}/2D_z = D$ , and  $B < \eta$ . The red solid and black thick lines denote the band touching and the Chern number change at high-symmetry points  $\Gamma$  and  $M$ , respectively. The outer boundary of the quantum paramagnet is determined when the band bottom touches zero energy at  $\Gamma$ .

where  $c_2(x) = (1+x)\ln^2(1+1/x) - \ln^2 x - 2\text{Li}_2(-x)$ ,  $\text{Li}_2(x)$  is the polylogarithm function,  $T$  is the average temperature,  $V$  is the volume of the material, and  $g(x) = [\exp(x/k_B T) - 1]^{-1}$  is the Bose-Einstein distribution. In Fig. 4(a), we show the dependence of  $\kappa_{xy}/k_B T$  on the temperature  $T$  with different DM interactions  $D$ . As we can infer from Eq. (26), because of the distribution function, the Berry curvature from lower bands contributes more to the thermal Hall conductivity. Therefore, the thermal Hall conductivity is large when  $D/J = 0.16$ , as the two lowest bands both have negative Chern numbers. Meanwhile, the thermal Hall conductivity is small in the case of  $D/J = 0.16$ , where the second-lowest band with a large positive Chern number  $+3$  suppresses the contribution of negative Berry curvature from the lowest band. Besides, if the temperature is getting higher, the occupations of the excitations in all six bands become more equally populated, and thus  $\kappa_{xy}$  goes closer to zero owing to the fact that  $\sum_{n,\mathbf{k}} \Omega_{n\mathbf{k}}^z = 0$ .

In experiments, the DM interaction is usually not tunable, and we thus depict a density plot of  $\kappa_{xy}/k_B T$  with respect to the magnetic field  $B$  and the temperature  $T$  in Fig. 4(b). With the lattice constant  $10 \text{ \AA}$  of  $\text{Tb}_2\text{Ti}_2\text{O}_7$  as an estimate for the interlayer distance  $l$ ,  $\kappa_{xy}/k_B T \sim 10^9 \text{ K}^{-1}\text{s}^{-1}$  gives rise to a bulk thermal Hall signal  $\kappa_{xy}/lT \sim 10^{-5} \text{ WK}^{-2}\text{m}^{-1}$ , in the same order as experimental measurements [12]. Due to the change of lower-band Berry curvature, with the magnetic field increasing, when the Chern numbers of the two lowest bands change from  $(-1, +3)$  to  $(-1, 0)$ , there is a sign flip of the thermal Hall conductivity around the critical field (denoted as the dotted black line). It should be pointed out that the phononic or extrinsic contribution to the sign change of thermal Hall effects in paramagnets is usually not tunable by the magnetic field or can be tuned limitedly accompanied by some magnetic phase transitions [51,52]. We expect the observation of this sign change can indicate the presence of

the upper branch thermal Hall effect, while a delicate experimental design may be needed to subtract the contribution from phonons as their effects are usually within the same order [14]. As we stated in the previous section, though we obtain the above results from a specific model on the kagomé lattice, the tunable thermal Hall signal arising from the topology of the excited multiplets can generally occur in various lattices.

## V. DISCUSSION

In this work, we have addressed the question of whether applying a Zeeman field to Mott insulators with multiple local energy levels could generate the intrinsic thermal Hall effect solely from the magnetic excitations in the quantum paramagnetic phase at finite temperatures. In our simple modeling, we have only considered the lowest a few CEF energy levels, which is sufficient to provide a positive answer. In reality, the candidate Mott insulators have many such CEF energy levels, and as the temperature increases, these CEF energy levels would be gradually thermally activated and contribute to thermal Hall transports. Thus, a comprehensive understanding of the thermal Hall signals in the candidate materials requires intrinsic components. Although here we focus on only the contribution of CEF excitations to the thermal Hall effects, we do not think phononic contribution should be ignored in any real materials. Based on our calculation, even in a simplified model, the thermal Hall conductivity from CEF excitations themselves is within the same order of the experimental result. We expect our results to be complementary to the recent efforts in phonon thermal Hall effects with the non-Kramers-like doublet systems [53,54]. The previous analysis on  $\text{Pr}_2\text{Ir}_2\text{O}_7$  has pointed out the resonant phonon-pseudospin scattering where the non-Kramers pseudospin arises from the ground-state doublet of the  $\text{Pr}^{3+}$  ion [14,54]. The inclusion of the upper branch CEF states not

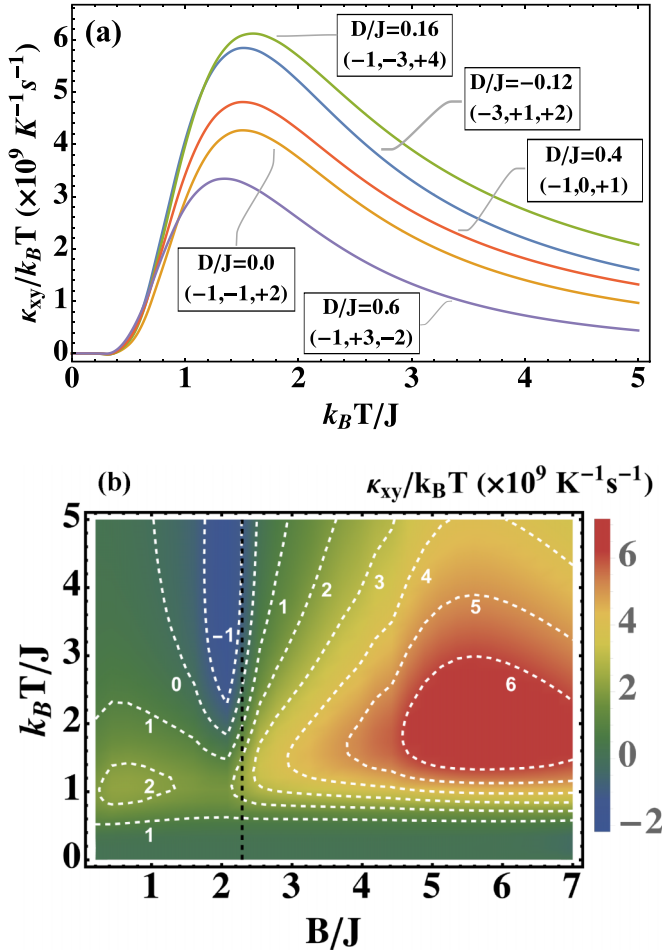


FIG. 4. The thermal Hall conductivity with varying parameters. We set  $\eta/J = 7.0$ ,  $\sqrt{3}D_p = \sqrt{3}/2D_z = D$ , and (a)  $B/J = 0.8$  with different values of  $D$  and the corresponding Chern numbers of the lower three bands labeled in the plot; (b)  $D/J = 0.9$  with the white numbers and dashed lines denoting the values of  $\kappa_{xy}/(k_B T)$  (in units of  $10^9 \text{ K}^{-1} \text{ s}^{-1}$ ). The black dashed line shows the critical field  $B_c/J \approx 2.3$  where the Chern numbers of the lower three bands change between  $(-1, +3, -2)$  and  $(-1, 0, +1)$ , resulting in a sign change of the thermal conductivity.

only generates the intrinsic thermal Hall sign as the upper branch thermal Hall effect, but may also induce a cascade of resonant phonon scattering with the large local Hilbert space [22].

In conventional ordered magnets, phonon-magnon hybridization [55–57] is known to create Berry curvature distribution for the hybridized excitations, and can also lead to nonzero magnetophonon chirality with thermal Hall effects [36,58]. This effect occurs even for the trivial magnon band structure that is absent of finite magnon Berry curvatures. For the exciton-like flavor-wave excitation in the quantum paramagnets, similar phonon-exciton hybridization could occur. Here, the flavor-wave excitation already develops Berry curvature distribution on its own. Thus, the hybridization could bring more interesting aspects to the dynamical properties of the whole system.

## ACKNOWLEDGMENTS

This work is supported by the National Science Foundation of China with Grant No. 92065203, the Ministry of Science and Technology of China with Grant No. 2021YFA1400300, and by the Research Grants Council of Hong Kong with Grants No. C6009-20G and No. C7012-21G.

## APPENDIX A: LINEAR FLAVOR-WAVE THEORY

In this section, we give the flavor-wave representation of effective spin. In the simple case that we discussed in the main text, the Hilbert space is spanned by states  $|f\rangle_i \equiv |\hat{\mathbf{z}}_i \cdot \mathbf{S}_i = |f\rangle$  with  $f = 0, \pm 1$  for each site  $i$ . Then, a set of  $SU(3)$  generators can be constructed as  $G_f^f(i) = |f\rangle_i \langle f'|_i$  with a normalization condition  $\sum_f |f\rangle_i \langle f'|_i = 1$ .

Under this basis, the spin ladder operators can be written as

$$S_i^+ = \sum_{ff'} \langle f|S_i^+|f'\rangle |f\rangle \langle f'| = \sqrt{2}[G_1^0(i) + G_0^1(i)] \quad (\text{A1})$$

$$S_i^- = \sum_{ff'} \langle f|S_i^-|f'\rangle |f\rangle \langle f'| = \sqrt{2}[G_1^0(i) + G_0^1(i)]. \quad (\text{A2})$$

Similarly,

$$S_i^z = \sum_{ff'} \langle f|S_i^z|f'\rangle |f\rangle \langle f'| = G_1^1(i) - G_1^{\bar{1}}(i) \quad (\text{A3})$$

$$(S_i^z)^2 = \sum_{ff'} \langle f|(S_i^z)^2|f'\rangle |f\rangle \langle f'| = G_1^1(i) + G_1^{\bar{1}}(i). \quad (\text{A4})$$

In the spirit of the flavor representations, the  $SU(3)$  algebra can be reproduced by two bosons  $b$  and  $\bar{b}$  as

$$G_1^1(i) = b_i^\dagger b_i, \quad (\text{A5})$$

$$G_1^{\bar{1}}(i) = \bar{b}_i^\dagger \bar{b}_i, \quad (\text{A6})$$

$$G_0^0(i) = 1 - b_i^\dagger b_i - \bar{b}_i^\dagger \bar{b}_i, \quad (\text{A7})$$

$$G_1^1(i) = \bar{b}_i^\dagger b_i, \quad (\text{A8})$$

$$G_1^0(i) = b_i^\dagger \sqrt{1 - b_i^\dagger b_i - \bar{b}_i^\dagger \bar{b}_i} \approx b_i^\dagger, \quad (\text{A9})$$

$$G_1^0(i) = \bar{b}_i^\dagger \sqrt{1 - b_i^\dagger b_i - \bar{b}_i^\dagger \bar{b}_i} \approx \bar{b}_i^\dagger. \quad (\text{A10})$$

With the above equations and  $G_f^f(i) = G_f^f(i)^\dagger$ , we immediately obtain the linear-flavor wave representation Eq. (5) in the main text.

## APPENDIX B: BOGOLIUBOV-DE GENNES HAMILTONIAN

In this section, we give the explicit form of the BdG Hamiltonian in the main text.

After the Fourier transform, we can obtain the BdG Hamiltonian that preserves particle-hole symmetry as

$$H = \frac{1}{2} \sum_{\mathbf{k}} \Psi_{\mathbf{k}}^\dagger H_{\mathbf{k}} \Psi_{\mathbf{k}} = \frac{1}{2} \sum_{\mathbf{k}} \Psi_{\mathbf{k}}^\dagger \begin{pmatrix} A_{\mathbf{k}} & B_{\mathbf{k}} \\ B_{-\mathbf{k}}^* & A_{-\mathbf{k}}^* \end{pmatrix} \Psi_{\mathbf{k}} \quad (\text{B1})$$

with

$$A_{\mathbf{k}} = -B \sin \theta I_3 \otimes \begin{pmatrix} 1 & 0 \\ 0 & -1 \end{pmatrix} + \begin{pmatrix} \eta & 0 & f_{3\mathbf{k}} & g_{3\mathbf{k}} & f_{2\mathbf{k}}^* & g_{2\mathbf{k}} \\ 0 & \eta & g_{3\mathbf{k}} & f_{3\mathbf{k}}^* & g_{2\mathbf{k}} & f_{2\mathbf{k}} \\ f_{3\mathbf{k}}^* & g_{3\mathbf{k}} & \eta & 0 & f_{1\mathbf{k}} & g_{1\mathbf{k}} \\ g_{3\mathbf{k}} & f_{3\mathbf{k}} & 0 & \eta & g_{1\mathbf{k}} & f_{1\mathbf{k}}^* \\ f_{2\mathbf{k}} & g_{2\mathbf{k}} & f_{1\mathbf{k}}^* & g_{1\mathbf{k}} & \eta & 0 \\ g_{2\mathbf{k}} & f_{2\mathbf{k}}^* & g_{1\mathbf{k}} & f_{1\mathbf{k}} & 0 & \eta \end{pmatrix} \quad (\text{B2})$$

and

$$B_{\mathbf{k}} = \begin{pmatrix} 0 & 0 & g_{3\mathbf{k}} & f_{3\mathbf{k}} & g_{2\mathbf{k}} & f_{2\mathbf{k}}^* \\ 0 & 0 & f_{3\mathbf{k}}^* & g_{3\mathbf{k}} & f_{2\mathbf{k}} & g_{2\mathbf{k}} \\ g_{3\mathbf{k}} & f_{3\mathbf{k}}^* & 0 & 0 & g_{1\mathbf{k}} & f_{1\mathbf{k}} \\ f_{3\mathbf{k}} & g_{3\mathbf{k}} & 0 & 0 & f_{1\mathbf{k}}^* & g_{1\mathbf{k}} \\ g_{2\mathbf{k}} & f_{2\mathbf{k}} & g_{1\mathbf{k}} & f_{1\mathbf{k}}^* & 0 & 0 \\ f_{2\mathbf{k}}^* & g_{2\mathbf{k}} & f_{1\mathbf{k}} & g_{1\mathbf{k}} & 0 & 0 \end{pmatrix}, \quad (\text{B3})$$

where

$$f_{m\mathbf{k}} = J \left[ \frac{1}{2} (1 - 3 \sin^2 \theta) - i\sqrt{3} \sin \theta \right] \cos(\mathbf{k} \cdot \boldsymbol{\delta}_m) + D_z \left[ \frac{\sqrt{3}}{2} (1 + \sin^2 \theta) - i \sin \theta \right] \cos(\mathbf{k} \cdot \boldsymbol{\delta}_m) - D_p [\sqrt{3} \sin \theta \cos \theta + i \cos \theta] \cos(\mathbf{k} \cdot \boldsymbol{\delta}_m), \quad (\text{B4})$$

$$g_{m\mathbf{k}} = \left[ \frac{3}{2} \left( J - \frac{1}{\sqrt{3}} D_z \right) \cos^2 \theta - \sqrt{3} D_p \cos \theta \sin \theta \right] \cos(\mathbf{k} \cdot \boldsymbol{\delta}_m), \quad (\text{B5})$$

and  $I_3$  the  $3 \times 3$  identity matrix.

Since the commutator gives

$$[\Psi_{\mathbf{k}}, \Psi_{\mathbf{k}}^\dagger] = \begin{pmatrix} 1 & 0 \\ 0 & -1 \end{pmatrix} \otimes I_{3 \times 3} \equiv \Sigma_z, \quad (\text{B6})$$

if we perform a Bogoliubov transformation  $\Psi_{\mathbf{k}} = T_{\mathbf{k}} \psi_{\mathbf{k}}$  to diagonalize  $H_{\mathbf{k}}$  while preserving the commutator, i.e.,  $[\psi_{\mathbf{k}}, \psi_{\mathbf{k}}^\dagger] = \Sigma_z$ , then

$$\Sigma_z = [\Psi_{\mathbf{k}}, \Psi_{\mathbf{k}}^\dagger] = T_{\mathbf{k}} [\psi_{\mathbf{k}}, \psi_{\mathbf{k}}^\dagger] T_{\mathbf{k}}^\dagger = T_{\mathbf{k}} \Sigma_z T_{\mathbf{k}}^\dagger, \quad (\text{B7})$$

$$T_{\mathbf{k}}^\dagger H_{\mathbf{k}} T_{\mathbf{k}} = \begin{pmatrix} E_{\mathbf{k}} & 0 \\ 0 & E_{-\mathbf{k}} \end{pmatrix}, \quad (\text{B8})$$

where  $E_{\mathbf{k}}$  is a  $6 \times 6$  diagonal matrix whose elements are the eigenenergies of the 6 bands respectively and  $E_{-\mathbf{k}}$  is the particle-hole symmetric partner of  $E_{\mathbf{k}}$ . As we mentioned in the main text, for any  $E_{\mathbf{k}}$ , the positiveness of the diagonal elements determines the mean-field phase diagram of this quantum paramagnetic phase, and we show the diagram in Fig. 5 with parameters  $\sin \theta = 1/3$ ,  $\sqrt{3}D_p = \sqrt{3}/2D_z = D$  as an example. Outside the yellow region,  $E_{\mathbf{k}} < 0$  for certain  $\mathbf{k}_0$ , and the system transits from the quantum paramagnetic phase into an ordered state with magnetic wave vector  $\mathbf{k}_0$ . In the main text, we focus on the  $\eta/J = 7$  cross section, as shown in Fig. 3.

It can also be checked that

$$i \frac{d}{dt} \psi_{\mathbf{k}} = [\psi_{\mathbf{k}}, H] = \Sigma_z H_{\mathbf{k}} \psi_{\mathbf{k}}, \quad (\text{B9})$$

and thus a proper Lagrangian should be

$$\mathcal{L}_{\mathbf{k}} = i \frac{d}{dt} - \Sigma_z H_{\mathbf{k}}. \quad (\text{B10})$$

Therefore, a bosonic vector potential  $\mathcal{A}_{n\mathbf{k}}$  and Berry curvature  $\Omega_{n\mathbf{k}}$  for  $\psi_{n\mathbf{k}}$  can be defined as [59]

$$\mathcal{A}_{n\mathbf{k}} = i \langle \psi_{n\mathbf{k}} | \Sigma_z \nabla_{\mathbf{k}} | \psi_{n\mathbf{k}} \rangle, \text{ and } \Omega_{n\mathbf{k}} = \nabla_{\mathbf{k}} \times \mathcal{A}_{n\mathbf{k}}. \quad (\text{B11})$$

In Fig. 6, we illustrate the Berry curvature distribution  $\Omega_{n\mathbf{k}}^z$  in the Brillouin zone with a specific parameter choice. These finite values of Berry curvature lead to the nonzero bosonic band Chern numbers that we discussed in the main text. We show the full diagram for all six band Chern numbers in Fig. 7.

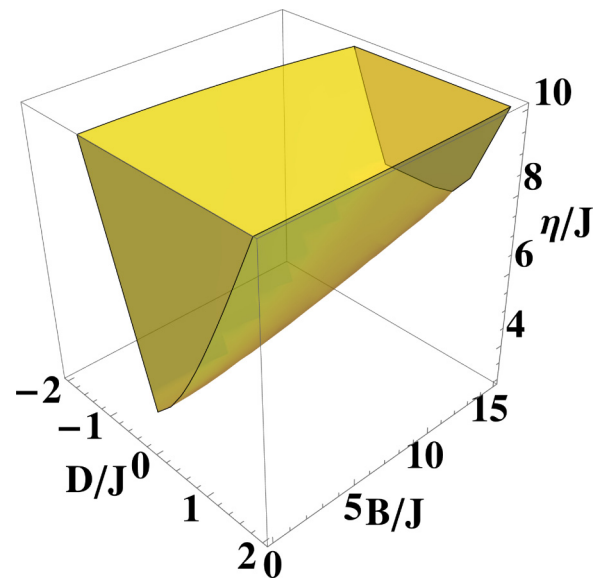


FIG. 5. (Color online.) The quantum paramagnetic phase (shown as yellow region) with  $\sin \theta = 1/3$  and  $\sqrt{3}D_p = \sqrt{3}/2D_z = D$ .

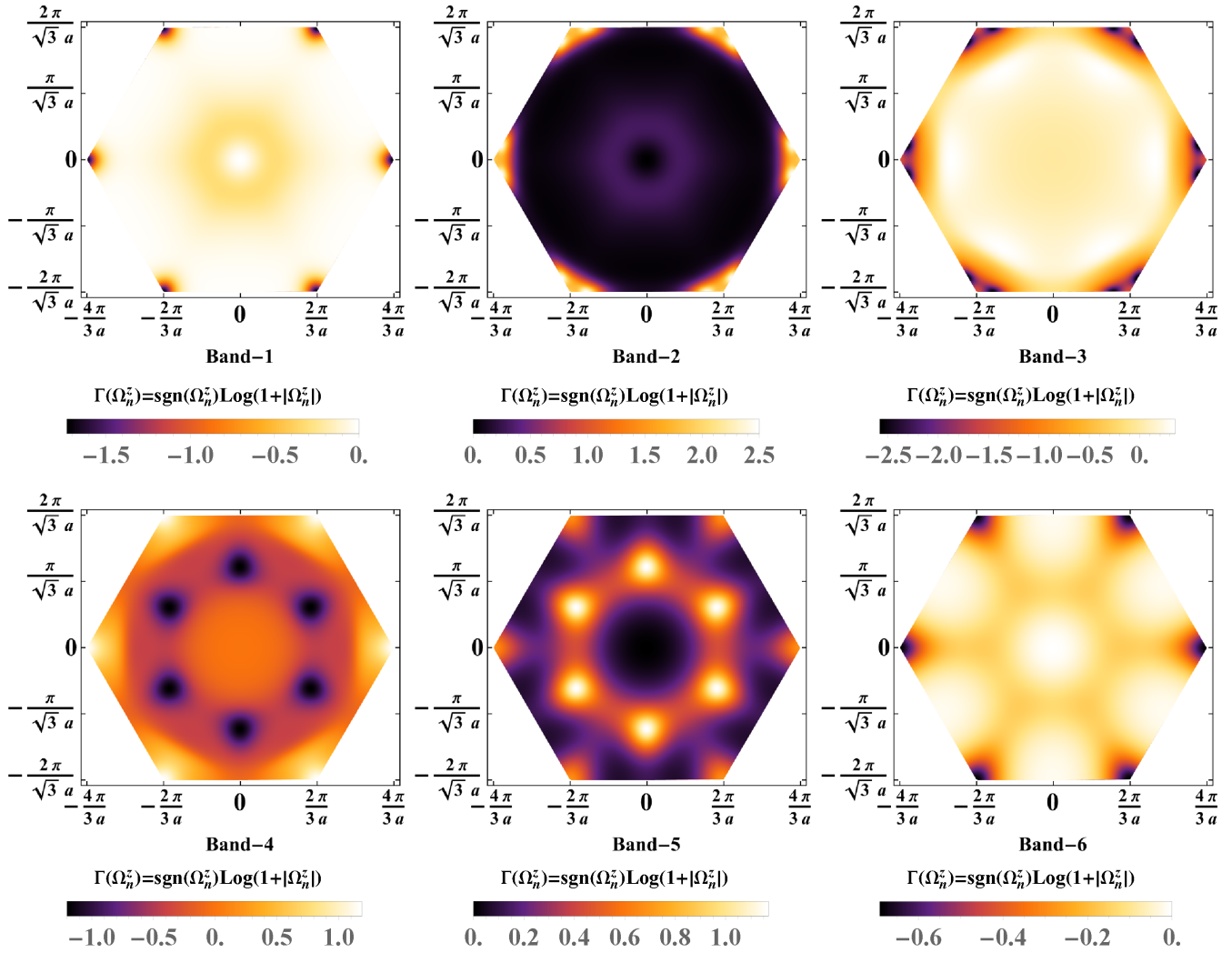


FIG. 6. The distribution of Berry curvature (in log scale) in the momentum space from the lowest band (band 1) to the highest band (band 6) with a parameter choice as  $\sin \theta = 1/3$ ,  $\eta/J = 7.0$ ,  $\sqrt{3}D_p = \sqrt{3}/2D_z = D$ , and  $B/J = 0.5$ .

### APPENDIX C: COLLINEAR CASE

In this section, we derive Eq. (13) in the main text. We first take  $\theta = \pi/2$  and  $D_p = 0$  into Eqs. (B1)–(B5), and to further simplify the expression, we then perform a gauge transformation as  $b_{m\mathbf{k}} \rightarrow ie^{-i\frac{2\pi m}{3}} b_{m\mathbf{k}}$  and  $\bar{b}_{m\mathbf{k}} \rightarrow -ie^{i\frac{2\pi m}{3}} \bar{b}_{m\mathbf{k}}$ . The  $12 \times 12$  Hamiltonian matrix in the basis  $\Psi_{\mathbf{k}} = (b_{1\mathbf{k}}, \bar{b}_{1\mathbf{k}}, \dots, b_{3\mathbf{k}}, \bar{b}_{3\mathbf{k}}, b_{1,-\mathbf{k}}, \bar{b}_{1,-\mathbf{k}}, \dots, b_{3,-\mathbf{k}}, \bar{b}_{3,-\mathbf{k}})^T$  is expressed as

$$H_{\mathbf{k}} = 2 \begin{pmatrix} \frac{\eta - B}{2} & 0 & \tilde{J} \cos \mathbf{k}_3 & 0 & \tilde{J}^* \cos \mathbf{k}_2 & 0 & 0 & 0 & 0 & \tilde{J} \cos \mathbf{k}_3 & 0 & \tilde{J}^* \cos \mathbf{k}_2 \\ 0 & \frac{\eta + B}{2} & 0 & \tilde{J}^* \cos \mathbf{k}_3 & 0 & \tilde{J} \cos \mathbf{k}_2 & 0 & 0 & \tilde{J}^* \cos \mathbf{k}_3 & 0 & \tilde{J} \cos \mathbf{k}_2 & 0 \\ \tilde{J}^* \cos \mathbf{k}_3 & 0 & \frac{\eta - B}{2} & 0 & \tilde{J} \cos \mathbf{k}_1 & 0 & 0 & \tilde{J}^* \cos \mathbf{k}_3 & 0 & 0 & 0 & \tilde{J} \cos \mathbf{k}_1 \\ 0 & \tilde{J} \cos \mathbf{k}_3 & 0 & \frac{\eta + B}{2} & 0 & \tilde{J}^* \cos \mathbf{k}_1 & \tilde{J} \cos \mathbf{k}_3 & 0 & 0 & 0 & \tilde{J}^* \cos \mathbf{k}_1 & 0 \\ \tilde{J} \cos \mathbf{k}_2 & 0 & \tilde{J}^* \cos \mathbf{k}_1 & 0 & \frac{\eta - B}{2} & 0 & 0 & \tilde{J} \cos \mathbf{k}_2 & 0 & \tilde{J}^* \cos \mathbf{k}_1 & 0 & 0 \\ 0 & \tilde{J}^* \cos \mathbf{k}_2 & 0 & \tilde{J} \cos \mathbf{k}_1 & 0 & \frac{\eta + B}{2} & \tilde{J}^* \cos \mathbf{k}_2 & 0 & \tilde{J} \cos \mathbf{k}_1 & 0 & 0 & 0 \\ 0 & 0 & 0 & \tilde{J}^* \cos \mathbf{k}_3 & 0 & \tilde{J} \cos \mathbf{k}_2 & \frac{\eta - B}{2} & 0 & \tilde{J}^* \cos \mathbf{k}_3 & 0 & \tilde{J} \cos \mathbf{k}_2 & 0 \\ 0 & 0 & \tilde{J} \cos \mathbf{k}_3 & 0 & \tilde{J}^* \cos \mathbf{k}_2 & 0 & 0 & \frac{\eta + B}{2} & 0 & \tilde{J} \cos \mathbf{k}_3 & 0 & \tilde{J}^* \cos \mathbf{k}_2 \\ 0 & \tilde{J} \cos \mathbf{k}_3 & 0 & 0 & 0 & \tilde{J}^* \cos \mathbf{k}_1 & \tilde{J} \cos \mathbf{k}_3 & 0 & \frac{\eta - B}{2} & 0 & \tilde{J}^* \cos \mathbf{k}_1 & 0 \\ \tilde{J}^* \cos \mathbf{k}_3 & 0 & 0 & 0 & \tilde{J} \cos \mathbf{k}_1 & 0 & 0 & \tilde{J}^* \cos \mathbf{k}_3 & 0 & \frac{\eta + B}{2} & 0 & \tilde{J} \cos \mathbf{k}_1 \\ 0 & \tilde{J}^* \cos \mathbf{k}_2 & 0 & \tilde{J} \cos \mathbf{k}_1 & 0 & 0 & \tilde{J}^* \cos \mathbf{k}_2 & 0 & \tilde{J} \cos \mathbf{k}_1 & 0 & \frac{\eta - B}{2} & 0 \\ \tilde{J} \cos \mathbf{k}_2 & 0 & \tilde{J}^* \cos \mathbf{k}_1 & 0 & 0 & 0 & 0 & \tilde{J} \cos \mathbf{k}_2 & 0 & \tilde{J}^* \cos \mathbf{k}_1 & 0 & \frac{\eta + B}{2} \end{pmatrix}. \quad (\text{C1})$$

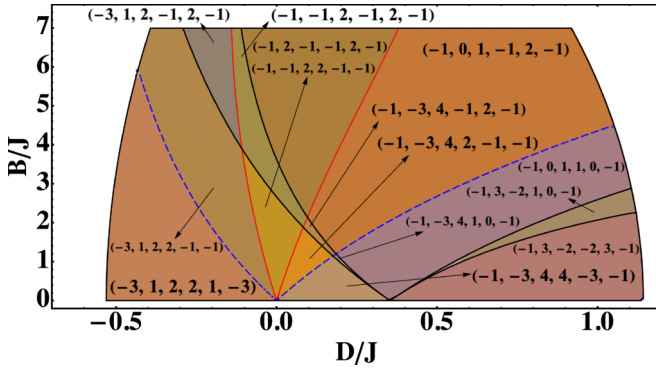


FIG. 7. Diagram of all six band Chern numbers distributions. The Chern numbers are listed from bottom to top. The parameters are the same as Fig. 3 in the main text. In addition to the band touching at  $\Gamma$  and  $\mathbf{M}$  denoted by the red solid and black thick lines, there is band-touching at  $\mathbf{K}$  denoted by blue dashed lines that gives rise to more complicated topological structures here.

Now, with the basis transformation that we mentioned in the main text,  $u_{m\mathbf{k}} = \frac{1}{\sqrt{2}}(b_{m\mathbf{k}} + \bar{b}_{m,-\mathbf{k}})$  and  $p_{m\mathbf{k}} = \frac{i}{\sqrt{2}}(\bar{b}_{m,-\mathbf{k}} - b_{m\mathbf{k}})$ , we can obtain  $H = \frac{1}{2} \sum_{\mathbf{k}} \Phi_{\mathbf{k}}^{\dagger} \tilde{H}_{\mathbf{k}} \Phi_{\mathbf{k}}$  with  $\Phi_{\mathbf{k}} = (u_{1\mathbf{k}}, \dots, u_{3\mathbf{k}}, p_{1\mathbf{k}}, \dots, p_{3\mathbf{k}}, u_{1,-\mathbf{k}}^{\dagger}, \dots, u_{3,-\mathbf{k}}^{\dagger}, p_{1,-\mathbf{k}}^{\dagger}, \dots, p_{3,-\mathbf{k}}^{\dagger})^T$ , where

$$\tilde{H}_{\mathbf{k}} = \begin{pmatrix} 2M_{\mathbf{k}} & -iBI_3 & 0 & 0 \\ iBI_3 & \eta I_3 & 0 & 0 \\ 0 & 0 & 2M_{\mathbf{k}}^* & iBI_3 \\ 0 & 0 & -iBI_3 & \eta I_3 \end{pmatrix}, \quad (\text{C2})$$

or alternatively,

$$H = \frac{1}{2(2\eta)^{-1}} \sum_{\mathbf{k}} (\mathbf{p}_{\mathbf{k}}^{\dagger} - i\frac{B}{\eta} \mathbf{u}_{\mathbf{k}}^{\dagger}) (\mathbf{p}_{\mathbf{k}} + i\frac{B}{\eta} \mathbf{u}_{\mathbf{k}}) + \frac{1}{2} \sum_{\mathbf{k}} \mathbf{u}_{\mathbf{k}}^{\dagger} (4M_{\mathbf{k}} - \frac{2B^2}{\eta}) \mathbf{u}_{\mathbf{k}} - B \quad (\text{C3})$$

as written in Eq. (13) of the main text (up to a constant), where we have used the fact that  $M_{\mathbf{k}} = M_{-\mathbf{k}} = M_{\mathbf{k}}^{\dagger}$  and  $[u_{m\mathbf{k}}^{\dagger}, p_{m'\mathbf{k}'}] = i\delta_{mm'}\delta_{\mathbf{k}\mathbf{k}'}$ . Here,  $I_3$  is the  $3 \times 3$  identity matrix.

Since  $M_{\mathbf{k}}$  is Hermitian, we can diagonalize  $2\eta M_{\mathbf{k}}$  by a unitary matrix  $Q_{\mathbf{k}}$  as

$$2\eta Q_{\mathbf{k}}^{\dagger} M_{\mathbf{k}} Q_{\mathbf{k}} = \text{Diag}(\tilde{E}_{1\mathbf{k}}^2, \tilde{E}_{2\mathbf{k}}^2, \tilde{E}_{3\mathbf{k}}^2) \equiv \tilde{E}_{\mathbf{k}}^2 \quad (\text{C4})$$

with  $Q_{\mathbf{k}}^{\dagger} Q_{\mathbf{k}} = I_3$ . Then, it can be found that

$$\tilde{Q}_{\mathbf{k}} = \begin{pmatrix} Q_{\mathbf{k}} \sqrt{\frac{\eta}{2\tilde{E}_{\mathbf{k}}}} & & & Q_{\mathbf{k}} \sqrt{\frac{\eta}{2\tilde{E}_{\mathbf{k}}}} \\ & Q_{\mathbf{k}}^* \sqrt{\frac{\eta}{2\tilde{E}_{\mathbf{k}}}} & Q_{\mathbf{k}}^* \sqrt{\frac{\eta}{2\tilde{E}_{\mathbf{k}}}} & \\ & -iQ_{\mathbf{k}}^* \sqrt{\frac{\tilde{E}_{\mathbf{k}}}{2\eta}} & iQ_{\mathbf{k}}^* \sqrt{\frac{\tilde{E}_{\mathbf{k}}}{2\eta}} & \\ -iQ_{\mathbf{k}} \sqrt{\frac{\tilde{E}_{\mathbf{k}}}{2\eta}} & & & iQ_{\mathbf{k}} \sqrt{\frac{\tilde{E}_{\mathbf{k}}}{2\eta}} \end{pmatrix} \quad (\text{C5})$$

can diagonalize  $\tilde{H}_{\mathbf{k}}$  as

$$\tilde{Q}_{\mathbf{k}}^{\dagger} \tilde{H}_{\mathbf{k}} \tilde{Q}_{\mathbf{k}} = \begin{pmatrix} \tilde{E}_{\mathbf{k}} - B & & & \\ & \tilde{E}_{\mathbf{k}} + B & & \\ & & \tilde{E}_{-\mathbf{k}} - B & \\ & & & \tilde{E}_{-\mathbf{k}} + B \end{pmatrix}, \quad (\text{C6})$$

while transforming the commutator

$$[\Phi_{\mathbf{k}}, \Phi_{\mathbf{k}}^{\dagger}] = I_2 \otimes \begin{pmatrix} 0 & i \\ -i & 0 \end{pmatrix} \otimes I_3 \quad (\text{C7})$$

into

$$\tilde{Q}_{\mathbf{k}}^{\dagger} [\Phi_{\mathbf{k}}, \Phi_{\mathbf{k}}^{\dagger}] \tilde{Q}_{\mathbf{k}} = \Sigma_z = \begin{pmatrix} 1 & 0 \\ 0 & -1 \end{pmatrix} \otimes I_6, \quad (\text{C8})$$

the canonical bosonic commutator with the particle (hole) eigenenergy

$$E_{\pm\mathbf{k}} = \begin{pmatrix} \tilde{E}_{\pm\mathbf{k}} - B & \\ & \tilde{E}_{\pm\mathbf{k}} + B \end{pmatrix}, \quad (\text{C9})$$

and thus  $\tilde{Q}_{\mathbf{k}}$  is the proper wave function for the phononic Hamiltonian Eq. (C2). It can be noticed that  $\tilde{Q}_{\mathbf{k}}$  fully depends on  $M_{\mathbf{k}}$  and does not change with nonzero  $B$ . Therefore, we have the conclusion in the main text that the topological properties of Hamiltonian  $H$  are fully determined by  $M_{\mathbf{k}}$ .

[1] X.-T. Zhang, Y. H. Gao, and G. Chen, Thermal Hall effects in quantum magnets, *Phys. Rep.* **1070**, 1 (2024).  
 [2] A. Kitaev, Anyons in an exactly solved model and beyond, *Ann. Phys.* **321**, 2 (2006).  
 [3] Y. Kasahara, T. Ohnishi, Y. Mizukami, O. Tanaka, S. Ma, K. Sugii, N. Kurita, H. Tanaka, J. Nasu, Y. Motome *et al.*, Majorana quantization and half-integer thermal quantum Hall effect in a Kitaev spin liquid, *Nature (London)* **559**, 227 (2018).  
 [4] T. Yokoi, S. Ma, Y. Kasahara, S. Kasahara, T. Shibauchi, N. Kurita, H. Tanaka, J. Nasu, Y. Motome, C. Hickey *et al.*, Half-integer quantized anomalous thermal Hall effect in the Kitaev material candidate  $\alpha$ -RuCl<sub>3</sub>, *Science* **373**, 568 (2021).  
 [5] Y. Onose, T. Ideue, H. Katsura, Y. Shiomi, N. Nagaosa, and Y. Tokura, Observation of the magnon Hall effect, *Science* **329**, 297 (2010).

[6] H. Katsura, N. Nagaosa, and P. A. Lee, Theory of the thermal Hall effect in quantum magnets, *Phys. Rev. Lett.* **104**, 066403 (2010).  
 [7] P. Laurell and G. A. Fiete, Magnon thermal Hall effect in kagome antiferromagnets with Dzyaloshinskii-Moriya interactions, *Phys. Rev. B* **98**, 094419 (2018).  
 [8] R. R. Neumann, A. Mook, J. Henk, and I. Mertig, Thermal Hall effect of magnons in collinear antiferromagnetic insulators: Signatures of magnetic and topological phase transitions, *Phys. Rev. Lett.* **128**, 117201 (2022).  
 [9] P. A. McClarty, Topological magnons: A review, *Annu. Rev. Condens. Matter Phys.* **13**, 171 (2022).  
 [10] J. Romhányi, K. Penc, and R. Ganesh, Hall effect of triplons in a dimerized quantum magnet, *Nat. Commun.* **6**, 6805 (2015).

- [11] P. A. McClarty, F. Krüger, T. Guidi, S. Parker, K. Refson, A. Parker, D. Prabhakaran, and R. Coldea, Topological triplon modes and bound states in a Shastry–Sutherland magnet, *Nat. Phys.* **13**, 736 (2017).
- [12] M. Hirschberger, J. W. Krizan, R. Cava, and N. Ong, Large thermal hall conductivity of neutral spin excitations in a frustrated quantum magnet, *Science* **348**, 106 (2015).
- [13] W. Chu and X. Sun, Low-temperature thermal Hall conductivity of  $\text{Pr}_2\text{Zr}_2\text{O}_7$  single crystal, [arXiv:2302.13300](https://arxiv.org/abs/2302.13300).
- [14] T. Uehara, T. Ohtsuki, M. Udagawa, S. Nakatsuji, and Y. Machida, Phonon thermal Hall effect in a metallic spin ice, *Nat. Commun.* **13**, 4604 (2022).
- [15] H. Yang, C. Kim, Y. Choi, J. H. Lee, G. Lin, J. Ma, M. Kratochvílová, P. Proschek, E.-G. Moon, K. H. Lee *et al.*, Significant thermal Hall effect in the  $3d$  cobalt Kitaev system  $\text{Na}_2\text{Co}_2\text{TeO}_6$ , *Phys. Rev. B* **106**, L081116 (2022).
- [16] H. Takeda, J. Mai, M. Akazawa, K. Tamura, J. Yan, K. Moovendaran, K. Raju, R. Sankar, K.-Y. Choi, and M. Yamashita, Planar thermal Hall effects in the Kitaev spin liquid candidate  $\text{Na}_2\text{Co}_2\text{TeO}_6$ , *Phys. Rev. Res.* **4**, L042035 (2022).
- [17] J. S. Gardner, M. J. P. Gingras, and J. E. Greedan, Magnetic pyrochlore oxides, *Rev. Mod. Phys.* **82**, 53 (2010).
- [18] J. S. Gardner, S. R. Dunsiger, B. D. Gaulin, M. J. P. Gingras, J. E. Greedan, R. F. Kiefl, M. D. Lumsden, W. A. MacFarlane, N. P. Raju, J. E. Sonier *et al.*, Cooperative paramagnetism in the geometrically frustrated pyrochlore antiferromagnet  $\text{Tb}_2\text{Ti}_2\text{O}_7$ , *Phys. Rev. Lett.* **82**, 1012 (1999).
- [19] H. R. Molavian, M. J. P. Gingras, and B. Canals, Dynamically induced frustration as a route to a quantum spin ice state in  $\text{Tb}_2\text{Ti}_2\text{O}_7$  via virtual crystal field excitations and quantum many-body effects, *Phys. Rev. Lett.* **98**, 157204 (2007).
- [20] S. Voleti, F. D. Wandler, and A. Paramakanti, Impact of gapped spin-orbit excitons on low energy pseudospin exchange interactions, *Phys. Rev. B* **109**, 094423 (2024).
- [21] X.-T. Zhang, Y. H. Gao, C. Liu, and G. Chen, Topological thermal Hall effect of magnetic monopoles in the pyrochlore  $U(1)$  spin liquid, *Phys. Rev. Res.* **2**, 013066 (2020).
- [22] G. V. Chen and C. Wu, Mott insulators with large local Hilbert spaces in quantum materials and ultracold atoms, *npj Quantum Mater.* **9**, 1 (2024).
- [23] G. Grissonnanche, A. Legros, S. Badoux, E. Lefrançois, V. Zlatko, M. Lizaire, F. Laliberté, A. Gourgout, J.-S. Zhou, S. Pyon *et al.*, Giant thermal Hall conductivity in the pseudogap phase of cuprate superconductors, *Nature (London)* **571**, 376 (2019).
- [24] M.-E. Boulanger, G. Grissonnanche, S. Badoux, A. Allaire, É. Lefrançois, A. Legros, A. Gourgout, M. Dion, C. Wang, X. Chen *et al.*, Thermal Hall conductivity in the cuprate Mott insulators  $\text{Nd}_2\text{CuO}_4$  and  $\text{Sr}_2\text{CuO}_2\text{Cl}_2$ , *Nat. Commun.* **11**, 5325 (2020).
- [25] P. S. Anisimov, F. Aust, G. Khaliullin, and M. Daghofer, Nontrivial triplon topology and triplon liquid in Kitaev-Heisenberg-type excitonic magnets, *Phys. Rev. Lett.* **122**, 177201 (2019).
- [26] C. Liu, F.-Y. Li, and G. Chen, Upper branch magnetism in quantum magnets: Collapses of excited levels and emergent selection rules, *Phys. Rev. B* **99**, 224407 (2019).
- [27] Z. L. Dun, J. Trinh, K. Li, M. Lee, K. W. Chen, R. Baumbach, Y. F. Hu, Y. X. Wang, E. S. Choi, B. S. Shastry *et al.*, Magnetic ground states of the rare-earth tripod Kagome lattice  $\text{Mg}_2\text{RE}_3\text{Sb}_3\text{O}_{14}$  ( $\text{RE} = \text{Gd}, \text{Dy}, \text{Er}$ ), *Phys. Rev. Lett.* **116**, 157201 (2016).
- [28] Z. Dun, X. Bai, J. A. M. Paddison, E. Hollingworth, N. P. Butch, C. D. Cruz, M. B. Stone, T. Hong, F. Demmel, M. Mourigal *et al.*, Quantum versus classical spin fragmentation in dipolar kagome ice  $\text{Ho}_3\text{Mg}_2\text{Sb}_3\text{O}_{14}$ , *Phys. Rev. X* **10**, 031069 (2020).
- [29] T. Moriya, Anisotropic superexchange interaction and weak ferromagnetism, *Phys. Rev.* **120**, 91 (1960).
- [30] I. Dzyaloshinsky, A thermodynamic theory of weak ferromagnetism of antiferromagnetics, *J. Phys. Chem. Solids* **4**, 241 (1958).
- [31] A. Joshi, M. Ma, F. Mila, D. N. Shi, and F. C. Zhang, Elementary excitations in magnetically ordered systems with orbital degeneracy, *Phys. Rev. B* **60**, 6584 (1999).
- [32] Y. Q. Li, M. Ma, D. N. Shi, and F. C. Zhang,  $SU(4)$  theory for spin systems with orbital degeneracy, *Phys. Rev. Lett.* **81**, 3527 (1998).
- [33] F.-Y. Li and G. Chen, Competing phases and topological excitations of spin-1 pyrochlore antiferromagnets, *Phys. Rev. B* **98**, 045109 (2018).
- [34] A. G. Del Maestro and M. J. Gingras, Quantum spin fluctuations in the dipolar Heisenberg-like rare earth pyrochlores, *J. Phys.: Condens. Matter* **16**, 3339 (2004).
- [35] B. Ma, B. Flebus, and G. A. Fiete, Longitudinal spin Seebeck effect in pyrochlore iridates with bulk and interfacial Dzyaloshinskii-Moriya interaction, *Phys. Rev. B* **101**, 035104 (2020).
- [36] B. Ma and G. A. Fiete, Antiferromagnetic insulators with tunable magnon-polaron Chern numbers induced by in-plane optical phonons, *Phys. Rev. B* **105**, L100402 (2022).
- [37] A. Mook, J. Henk, and I. Mertig, Edge states in topological magnon insulators, *Phys. Rev. B* **90**, 024412 (2014).
- [38] S. K. Kim, H. Ochoa, R. Zarzuela, and Y. Tserkovnyak, Realization of the Haldane-Kane-Mele model in a system of localized spins, *Phys. Rev. Lett.* **117**, 227201 (2016).
- [39] S. Owerre, A first theoretical realization of honeycomb topological magnon insulator, *J. Phys.: Condens. Matter* **28**, 386001 (2016).
- [40] K. Ohgushi, S. Murakami, and N. Nagaosa, Spin anisotropy and quantum Hall effect in the kagomé lattice: Chiral spin state based on a ferromagnet, *Phys. Rev. B* **62**, R6065 (2000).
- [41] R. Barnett, G. R. Boyd, and V. Galitski,  $SU(3)$  spin-orbit coupling in systems of ultracold atoms, *Phys. Rev. Lett.* **109**, 235308 (2012).
- [42] T. Fukui, Y. Hatsugai, and H. Suzuki, Chern numbers in discretized Brillouin zone: Efficient method of computing (spin) Hall conductances, *J. Phys. Soc. Jpn.* **74**, 1674 (2005).
- [43] R. Ganesh, D. N. Sheng, Y.-J. Kim, and A. Paramakanti, Quantum paramagnetic ground states on the honeycomb lattice and field-induced Néel order, *Phys. Rev. B* **83**, 144414 (2011).
- [44] R. Moessner, O. Tchernyshyov, and S. L. Sondhi, Planar pyrochlore, quantum ice and sliding ice, *J. Stat. Phys.* **116**, 755 (2004).
- [45] M. Sadrzadeh, R. Haghshenas, and A. Langari, Quantum phase diagram of the two-dimensional transverse-field Ising model: Unconstrained tree tensor network and mapping analysis, *Phys. Rev. B* **99**, 144414 (2019).
- [46] X. Hu, A. Rüegg, and G. A. Fiete, Topological phases in layered pyrochlore oxide thin films along the  $[111]$  direction, *Phys. Rev. B* **86**, 235141 (2012).

- [47] D. Xiao, M.-C. Chang, and Q. Niu, Berry phase effects on electronic properties, *Rev. Mod. Phys.* **82**, 1959 (2010).
- [48] R. Cheng, S. Okamoto, and D. Xiao, Spin Nernst effect of magnons in collinear antiferromagnets, *Phys. Rev. Lett.* **117**, 217202 (2016).
- [49] R. Matsumoto and S. Murakami, Rotational motion of magnons and the thermal Hall effect, *Phys. Rev. B* **84**, 184406 (2011).
- [50] R. Matsumoto and S. Murakami, Theoretical prediction of a rotating magnon wave packet in ferromagnets, *Phys. Rev. Lett.* **106**, 197202 (2011).
- [51] L. Chen, M.-E. Boulanger, Z.-C. Wang, F. Tafti, and L. Taillefer, Large phonon thermal Hall conductivity in the antiferromagnetic insulator  $\text{Cu}_3\text{TeO}_6$ , *Proc. Natl. Acad. Sci. USA* **119**, e2208016119 (2022).
- [52] X. Li, Y. Machida, A. Subedi, Z. Zhu, L. Li, and K. Behnia, The phonon thermal Hall angle in black phosphorus, *Nat. Commun.* **14**, 1027 (2023).
- [53] H. Guo, D. G. Joshi, and S. Sachdev, Resonant thermal Hall effect of phonons coupled to dynamical defects, *Proc. Natl. Acad. Sci. USA* **119**, e2215141119 (2022).
- [54] H. Guo, Phonon thermal Hall effect in a non-Kramers paramagnet, *Phys. Rev. Res.* **5**, 033197 (2023).
- [55] X. Zhang, Y. Zhang, S. Okamoto, and D. Xiao, Thermal Hall effect induced by magnon-phonon interactions, *Phys. Rev. Lett.* **123**, 167202 (2019).
- [56] G. Go, S. K. Kim, and K.-J. Lee, Topological magnon-phonon hybrid excitations in two-dimensional ferromagnets with tunable Chern numbers, *Phys. Rev. Lett.* **123**, 237207 (2019).
- [57] S. Zhang, G. Go, K.-J. Lee, and S. K. Kim,  $\text{SU}(3)$  topology of magnon-phonon hybridization in 2D antiferromagnets, *Phys. Rev. Lett.* **124**, 147204 (2020).
- [58] B. Ma, Z. Wang, and G. Chen, Chiral magneto-phonons with tunable topology in anisotropic quantum magnets, [arXiv:2309.04064](https://arxiv.org/abs/2309.04064).
- [59] B. A. Bernevig, *Topological Insulators and Topological Superconductors* (Princeton University, Princeton, 2013).